Magnetic Resonance Materials in Physics, Biology and Medicine (2018) 31:747–756
https://doi.org/10.1007/s10334-018-0694-8

RESEARCH ARTICLE

Improved 4D cardiac functional assessment for pediatric patients using motion-weighted image reconstruction

Ziwu Zhou[1,2] · Fei Han[1,2] · Takegawa Yoshida[1] · Kim-Lien Nguyen[1,4] · John Paul Finn[1,3] · Peng Hu[1,3,5]

Received: 19 April 2018 / Revised: 6 July 2018 / Accepted: 8 July 2018 / Published online: 24 July 2018

Abstract

Objective Our aim was to develop and evaluate a motion-weighted reconstruction technique for improved cardiac function assessment in 4D magnetic resonance imaging (MRI).

Materials and methods A flat-topped, two-sided Gaussian kernel was used to weigh k-space data in each target cardiac phase and adjacent two temporal phases during the proposed phase-by-phase reconstruction algorithm. The proposed method (Strategy 3) was used to reconstruct 18 cardiac phases based on data acquired using a previously proposed technique [4D multiphase steady-state imaging with contrast enhancement (MUSIC) technique and its self-gated extension using rotating Cartesian k-space (ROCK-MUSIC) from 12 pediatric patients. As a comparison, the same data set was reconstructed into nine phases using a phase-by-phase method (Strategy 1), 18 phases using view sharing (Strategy 4), and 18 phases using a temporal regularized method (Strategy 2). Regional image sharpness and left ventricle volumetric measurements were used to compare the four reconstructions quantitatively.

Results Strategies 1 and 4 generated significantly sharper images of static structures ($P \leq 0.018$) than Strategies 2 and 3 but significantly more blurry ($P \leq 0.021$) images of the heart. Left ventricular volumetric measurements from the nine-phase reconstruction (Strategy 1) correlated moderately ($r < 0.8$) with the 2D cine, whereas the remaining three techniques had a higher correlation ($r > 0.9$). The computational burden of Strategy 2 was six times that of Strategy 3.

Conclusion The proposed method of motion-weighted reconstruction improves temporal resolution in 4D cardiac imaging with a clinically practical workflow.

Keywords Motion compensation · Regularized reconstruction · Soft-gating · Pediatric patient

Introduction

Cardiac magnetic resonnce imaging (MRI) (CMR) is widely used for assessing cardiac structure and function over a spectrum of disorders, including pediatric congenital heart disease (CHD) [1–3]. Conventionally, a stack of 2D cine images is acquired in sequential breath-holds to generate parameters related to cardiac function, including left and right ventricular volumes, myocardial mass, and ejection fraction. Although considered the clinical standard in adults, breath-held 2D cine has limitations for pediatric patients with CHD. First, slices are relatively thick (3–5 mm), while the requirement for high spatial resolution is demanding in small children due to the diminutive size of the heart. Additionally, repeated breath-holding and prolonged anesthesia are undesirable in many small children with CHD due to the risk of arterial desaturation [4].

✉ Peng Hu
penghu@mednet.ucla.edu

1 Department of Radiological Sciences, David Geffen School of Medicine, University of California, Los Angeles, CA, USA

2 Department of Bioengineering, University of California, Los Angeles, CA, USA

3 Biomedical Physics Inter-Departmental Graduate Program, University of California, Los Angeles, CA, USA

4 Division of Cardiology, VA Greater Los Angeles Healthcare System, Los Angeles, CA, USA

5 Department of Radiological Sciences, David Geffen School of Medicine, University of California, 300 UCLA Medical Plaza Suite B119, Los Angeles, CA 90095, USA

The recently proposed 4D multiphase steady-state imaging with contrast enhancement (MUSIC) technique [5] and its self-gated extension using rotating Cartesian k-space (ROCK-MUSIC) [6], have addressed several limitations that previously challenged cardiac imaging in pediatric CHD. By generating 4D images with isotropic high spatial resolution, without the requirement for breath-holding or slice positioning, MUSIC and ROCK-MUSIC have opened new vistas for speedy and definitive diagnosis, even in tiny patients with the most complex CHD anatomy [7].

When performed in combination with ferumoxytol administration, the signal from the blood pool on 4D MUSIC is bright and uniform, facilitating segmentation of dynamic ventricular volumes for functional analysis. However, implementations of 4D MUSIC and ROCK-MUSIC generate about nine cardiac phases in 8 and 5 min, respectively. Whereas this is sufficient for detailed cardiac and vascular anatomy, the temporal resolution for functional analysis is poor compared with 2D cine, where 20–30 cardiac phases are routine. Therefore, improved temporal resolution is desirable for more detailed cardiac functional evaluation based on 4D MUSIC or ROCK-MUSIC.

The k-space sampling pattern in the ROCK-MUSIC technique allows for retrospective data binning into an arbitrary number of cardiac phases. Given the same amount of data, increasing the number of cardiac phases means fewer k-space samples for each cardiac phase. To address this issue, algorithms that exploit the temporal correlation of the data set are usually used to reconstruct the highly undersampled k-space [8–12]. Motion-regularized methods reconstruct images of all the motion states (i.e., cardiac phases) in a single optimization process and impose a regularization term on the sparsifying transformation along the motion direction [13–16]. Although motion-regularized methods could reconstruct highly undersampled dynamic k-space data, the fact that all the images of different motion states are reconstructed in a joint optimization process significantly increases the computational burden and computer memory requirement [17–19].

Motion-weighted image reconstruction is a recently proposed alternative approach to reconstructing highly undersampled, motion-corrupted k-space data. Instead of introducing additional regularization terms, the motion-weighted methods add a weighting $w \in [0, 1]$ to the data consistency term of the compressed sensing-type reconstruction based on the degree of motion that occurred. Since the degree of motion corruption is described using the full range of [0, 1], this scheme is also called motion soft-gating. The concept was first introduced by Johnson et al. [20] where the weightings were based on the degree of off-resonance and later applied in free-breathing coronary MR angiography (MRA) [21], abdominal imaging [22], dynamic contrast-enhanced MRI [23], cardiac imaging [6], and pulmonary MRI [18] to suppress respiratory motion. One advantage of the motion-weighted method is that image reconstruction is independent for each motion state, which not only significantly reduces the computation scale of the problem but also allows for parallelized implementation.

In this study, we used a motion-regularized method, a motion-weighted method, and a view-sharing method to improve the temporal resolution of previously acquired ROCK-MUSIC data sets [6]. The high-temporal-resolution 4D images (18 cardiac phases) reconstructed by the aforementioned three methods were compared with low-temporal-resolution (9 cardiac phases) images reconstructed without these methods in terms of image quality and sharpness. Left ventricular (LV) functional measurements based on the four sets of reconstructed 4D images were validated against the measurements based on 2D cine.

Materials and methods

Data preparation

This study included 12 pediatric CHD patients who underwent ferumoxytol-enhanced CMR exams on a 3.0-T whole-body scanner (Magnetom TIM Trio, Siemens Healthcare Solutions) during uninterrupted positive-pressure ventilation. Study population details are summarized in Tables 1 and 2. The study was approved by our institutional review board, and written informed consent was obtained before each MRI scan. The CMR protocol included both ROCK-MUSIC (TE/TR = 1.2 ms/2.9 ms, matrix size $480 \times 280 \times 140$, 0.8–1 mm^3 isotropic resolution, total acquisition time = 6 min, FA = 20°) and multiple 2D cine covering the left ventricle in cardiac short axis [TE/TR = 1.8/3.6 ms, 12 s ventilator-controlled breath-holds, 1-mm in-plane resolution, 5-mm slice thickness, 25 cardiac phases, echocardiogram (ECG) gated].

Image reconstruction

In the original ROCK-MUSIC [6], all acquired k-space data, regardless of respiratory motion state, were included in the image reconstruction in order to achieve a 100% efficiency. In this study, to focus solely on resolving cardiac motion in all comparing strategies mentioned below, the acquired ROCK-MUSIC k-space data first underwent a retrospective respiratory gating by discarding the k-space data points in which corresponding respiratory positions, derived from the extracted self-gated respiratory signal using k-space center lines [6], were outside a predetermined gating acceptance window. The window size was set to 40% of the self-gated respiratory signal's dynamic

Table 1 Demographics of patient population

	Mean ± SD	Range
Gender	8 males, 4 females	
Age	4.1 ± 3.7 years	2 days–8 years
Heart rate (bpm)	102.6 ± 14.3	90–145
Weight (kg)	14.0 ± 5.1	3–22.5
		Percent (no.)
Tetralogy of fallot		33.3% (4)
Hypoplastic aortic arch		16.7% (2)
Aortic coarctation		16.7% (2)
Transposition of great arteries		8.3% (1)
Ventricular septal defect		25% (3)

range and its location set to end-expiration. After respiratory gating, each data set was then reconstructed using the four strategies:

Strategy 1: Data were binned into nine cardiac phases and reconstructed phase by phase with an algorithm using combined standard parallel imaging and compressed sensing with spatial wavelet regularization only [24, 25]:

$$\hat{d} = \arg\min \sum_{i=1}^{N} ||\left|D\mathcal{F}S_i d - m_i\right||_2^2 + \lambda_1 ||R_1 d||_1. \quad (1)$$

Strategy 2: Data were binned into 18 cardiac phases and reconstructed using cardiac motion-regularized reconstruction, which can be generally described as follows [26, 27]:

$$\hat{d} = \arg\min_{d} \sum_{i=1}^{N} ||\left|D\mathcal{F}S_i d - m_i\right||_2^2 + \lambda_1 ||R_1 d||_1 + \lambda_2 ||R_2 d||_1, \quad (2)$$

where $\mathcal{F}$ is the Fourier transform; S_i are the sensitivity maps; D is the operator that selects locations where data have been acquired; d is the multiphase images to be reconstructed; m_i is the acquired undersampled k-space data from each of the N receiver coil elements; R_1 R_2 are spatial and temporal sparsifying transforms, respectively; and λ_1 and λ_2 are corresponding regularization parameters. One of the popular choices for temporal regularization R_2 in cardiac imaging is total variation, which assumes that cardiac motion (i.e., contraction and relaxation) is smooth and continuous across the cardiac cycle. In this study, we chose R_1 to be spatial wavelets and R_2 to be temporal total variation.

Strategy 3: Data were first separated into 18 bins, as shown in Fig. 1a. A flat-topped, two-sided Gaussian kernel that slides through each bin was then generated and used to weigh each data point residing under the kernel. Specifically, the flat-topped Gaussian kernel was scaled with the maximum set to 1 and centered at each bin, with the duration of the flat top equal to the duration of the target bin and the duration of ramps on each side equal to half of the duration of adjacent bins. The parameters [mean and standard deviation (SD)] of the Gaussian ramps were designed such that they decay to half strength at 50% of their duration. A schematic plot of this Gaussian kernel is shown in Fig. 1b. Finally, the acquired data and corresponding weights were grouped into individual cardiac phases (18 in total), as shown in Fig. 1c, and reconstructed phase by phase using the motion-weighted reconstruction, which can be modified from Eq. 2, as follows [21–23]:

$$\hat{d}_{\mathrm{p}} = \arg\min_{d_{\mathrm{p}}} \sum_{i=1}^{N} ||\left|W(D\mathcal{F}S_i d_{\mathrm{p}} - M_i)\right||_2^2 + \lambda_1 ||R_1 d_{\mathrm{p}}||_1, \quad (3)$$

where d_{p} is the image of target phase; M_i is the multicoil k-space data of the target phase and two adjacent phases; and W is the diagonal matrix containing the weight for each data point. The solution of this motion-weighted reconstruction converges toward the target phase, and the temporal blurring caused by incorporating data from the adjacent cardiac phases is inherently suppressed in the reconstruction process. R_1 is also set to be spatial wavelets.

Strategy 4: All nonzero values of the weighting matrix W used in Strategy 3 were replaced with 1, making Strategy 4 identical to a conventional view-sharing/sliding-window reconstruction [28] that reconstructs 18 temporal frames based on the 4D data sets, where the temporal footprint of each temporal frame is twice as long as the temporal sampling period of the dynamic image. All reconstructions were performed on a custom-build Linux PC (4 core/4 GHz, 64 GB memory, Nvidia GTX 760) with parallelized CPU and GPU acceleration using C++ and the BART toolbox [29]. Image reconstruction time for each strategy was recorded.

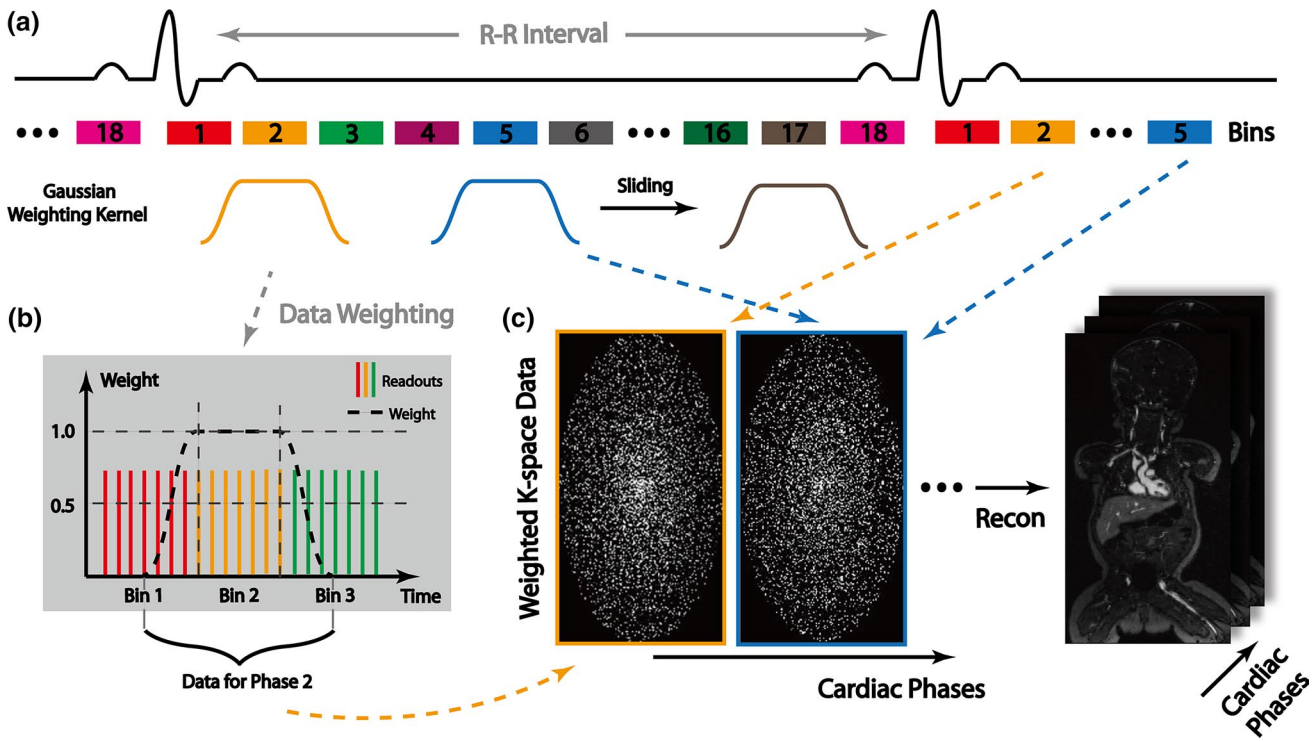

Fig. 1 Motion-weighted image reconstruction (Strategy 3). **a** Acquired data were first evenly separated into 18 bins. A Gaussian weighting kernel that slides through each bin was then used to weigh readouts that reside under the kernel. **b** Specifically, the weighting kernel has a flat top over the duration of the target bin, and the duration of the ramps on either side equals half of the duration for the adjacent bins. Weight equals to 1 was assigned to readouts under the flat top, while progressively decaying weights were assigned to readouts under the side ramps. **c** Finally, the acquired data and corresponding weights were grouped into 18 cardiac phases and input into a phase-by-phase parallel imaging and compressed sensing combined reconstruction algorithm

Image analysis

Regional image sharpness measurements were calculated using gradient entropy, a metric highly correlated with observed image sharpness [30]. To evaluate the effect of motion on image sharpness, gradient entropy was computed for two regions of interest (ROIs), as shown in Fig. 4a: the common carotid arteries (CCA, static tissue), and the entire heart (nonstatic tissue). For each region, gradient entropy was computed separately for each cardiac phase and averaged across all phases. The 3D rectangular ROIs were defined manually, and the selected pixel data were processed using an in-house MATLAB program.

Left ventricle end-systolic volume (ESV), end-diastolic volume (EDV), and ejection fraction (EF) were measured based on images reconstructed using the four strategies and the gold standard 2D cine. The 4D data sets were reformatted into the same slice orientations as the 2D cine images, and the left ventricle was manually contoured using a commercially available software (QMass, Medis, The Netherlands) by the same observer for all images.

Statistical analysis

Quantitative gradient-entropy-based image sharpness was compared in two steps after satisfying normality assumption: First, a one-way analysis of variance (ANOVA) test was used to test the differences among all four reconstructions; Second, if significant difference was found among the techniques, a post hoc Tukey's honest significant difference (HSD) test was performed for each of the six pairs of strategies. Both one-way ANOVA and Tukey's HSD were performed separately for the two ROIs (CCA and the heart) using a Bonferroni correction ($P < 0.05/2 = 0.025$). The EDV, ESV, and EF measurements from the four reconstruction strategies were compared with measurements from cine images using Lin's concordance correlation coefficient [31].

Results

All retrospective reconstructions were completed successfully. Reconstruction time was 0.73 ± 0.15 min per phase for Strategy 1, 4.1 ± 0.36 min on average per phase for

Strategy 2, 0.72 ± 0.18 min per phase for Strategy 3, and 0.72 ± 0.09 min per phase for Strategy 4. Figure 2 shows representative images of the four reconstruction strategies from a 6-year-old, 6.2 kg female patient. Figure 2a, b are two different coronal view slices at two different cardiac phases. Fine intracardiac structures, such as the papillary muscles and their connections (black and red arrowheads) were more clearly defined in Strategies 2 and 3 than with Strategies 1 and 4 due to the lower temporal resolution for nine-phase reconstruction and longer temporal footprint for view-sharing reconstruction, respectively. With lower effective undersampling (more data are used for each phase) in Strategy 3, the reconstructed images had slightly lower background noise and sharper delineation of fine structures compared with Strategy 2.

The high temporal resolution from reconstructions with Strategies 2 and 3 may be helpful for clearer visualization of major coronary arteries. Figure 3 shows the right coronary artery (RCA) and left anterior descending artery (LAD) in a 4-year-old, 4.8-kg male patient. Due to the long temporal footprint of view-sharing reconstruction in Strategy 4, both the RCA and LAD are blurred by the cardiac motion (red arrows). This is also true for the low temporal resolution reconstruction in Strategy 1, where RCA and LAD are not clearly depicted (yellow arrows). Conversely, the true short temporal footprint reconstructions from Strategies 2 and 3 enabled clear visualization of these coronary arteries.

Figure 4a demonstrates the two ROIs that are used to determine image sharpness in an exemplary image. As shown in Fig. 4b, mean sharpness scores (± SD) of the four reconstruction strategies were 0.693 ± 0.027, 0.538 ± 0.013, 0.543 ± 0.011, and 0.705 ± 0.022, respectively, in the CCA. Image sharpness was significantly different among the four techniques ($P = 0.008$). Furthermore, Strategies 1 and 4 showed significantly improved image sharpness than the other two strategies for the CCA ($P \leq 0.018$ for all comparisons) but not a significant difference among themselves. This is because more data are included in the image reconstruction in Strategies 1 and 4, which translate to higher spatial resolution. However, in the heart region, Strategies 2 and 3 reconstruct significantly sharper images than Strategies 1 and 4 (0.309 ± 0.011, 0.389 ± 0.008, 0.392 ± 0.006, and 0.323 ± 0.012, respectively; $P = 0.016$ for global comparison, $P < 0.02$ for all paired comparisons between Strategies 2 and 3 and 1 and 4). This is because the spatial resolution advantage of Strategies 1 and 4 was compromised by the cardiac motion blurring resulting from their lower temporal resolution. Such compromise is more severe in the pediatric application, where patients usually have high heart rate (> 100 bpm).

Because the reconstructed 4D images from MUSIC and ROCK-MUSIC can be reformatted into any user-specified slice orientation, the images were reformatted into ventricular short-axis views similar to those prescribed for

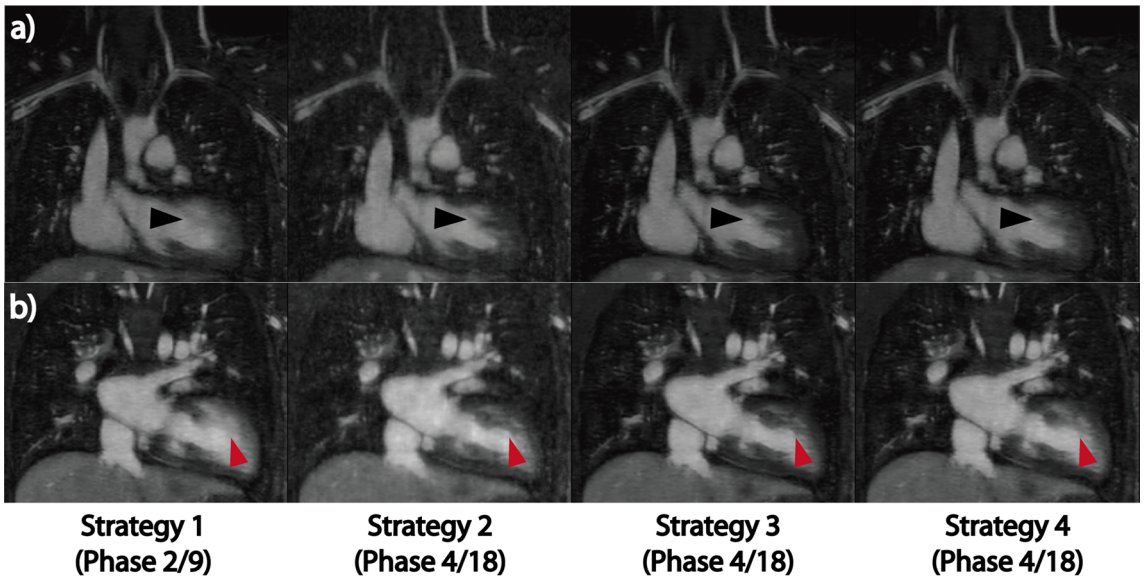

Fig. 2 Reconstructed 4D images using the four different strategies on the same data set acquired on a 6-year-old female patient. **a**, **b** show two different coronal view slices at two different cardiac phases. Low-temporal-resolution reconstruction in Strategy 1 results in motion-blurred intracardiac structures, such as the papillary muscles and their connections (black and red arrowheads). Using view sharing in Strategy 4 can improve the temporal resolution, which leads to slightly sharper delineation of these fine structures. However, the temporal footprint in Strategy 4 remained the same as in Strategy 1. With a true higher temporal resolution and temporal footprint reconstruction in Strategy 2 and 3, cardiac motion is nicely resolved, with well-defined intracardiac structures

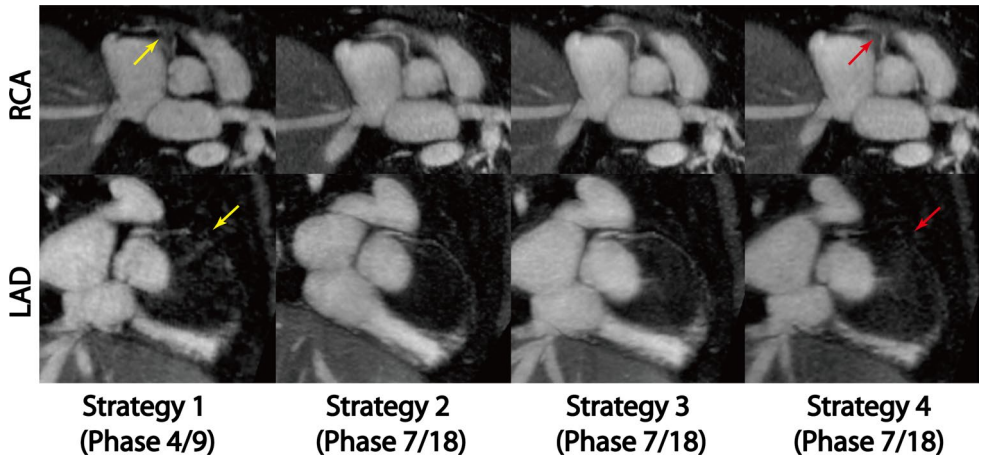

Fig. 3 Multiplanar reformatted images of the coronary arteries from a 4-year-old male patient using the four reconstruction strategies. The long temporal footprint using view-sharing reconstruction (Strategy 4) precludes visualization of the full length and course of the right coronary (RCA) and left anterior descending (LAD) arteries (red arrows). Similarly, the low temporal resolution reconstruction in Strategy 1 cannot clearly depict these arteries (yellow arrows). On the other hand, strategies with shorter temporal footprints (Strategies 2 and 3) allow sharper visualization and clearer course of these structures

2D cine. Figure 5 shows images in multiple selected cardiac phases. The M-Mode plot, which shows the signal along a chosen ultrasound line as a function of time, at the level of the blue dotted line is shown at the right to enable visual comparison of the temporal resolution of reconstruction strategies. The limited temporal resolution of Strategy 1 resulted in a coarse temporal profile, while the remaining three strategies provided smoother profiles over time, similar to 2D cine.

Table 2 summarizes the quantitative LV functional measurements, including ESV, EDV, and EF based on the four different reconstruction strategies, with values from 2D cine as the reference standard. The measurements based on images with low temporal resolution (nine phases, Strategy 1) have a systemic 8% overestimation of ESV and ~2% underestimation of EDV compared with measurements based on 2D cine. These errors resulted in a 7% underestimation of EF. Measurements based on images with high temporal resolution (18 phases, Strategies 2, 3, and 4) had much smaller errors ($\leq$4.1%) based on 2D cine values. There were minimal differences between Strategies 2, 3, and 4 in terms of quantitative LV functional measurement. All these observations are also reflected in Lin's correlation coefficient shown in Table 2.

Discussion

In this study, we evaluated four different image reconstruction strategies all aiming to improve the number of reconstructed cardiac phases of the 4D ROCK-MUSIC data set for improved cardiac function assessment. In quantitative regional image sharpness, we found obvious improvements using the high-temporal-resolution reconstruction with Strategies 2 and 3 compared with the phase-by-phase reconstruction or the view-sharing reconstruction. However, there were no significant differences between Strategies 2 and 3 other than reconstruction time and memory usage. The proposed Strategy 3 requires a shorter reconstruction time than Strategy 2. In our implementation, 4D images with 18 cardiac phases can be reconstructed within 10 min and 23 GB of memory using the motion-weighted reconstruction method, while >2 h and 60 GB of memory is required when using the motion-regularized reconstruction method with the same computer hardware. Based on these findings, the motion-weighted reconstruction method represents a time-and computational-efficient solution for improving cardiac function assessment based on 4D ROCK-MUSIC. Our solution for image reconstruction based on motion weighing is practical and can be easily implemented in clinical practice.

The motion-weighted image reconstruction is different from view sharing, which directly includes k-space data from other motion states or temporal frames into the image reconstruction. The increased temporal footprint of view sharing will result in motion blurring in the reconstructed images. On the other hand, motion-weighted reconstruction offers an additional "relaxed" subsampling operation where the reconstruction will directly use k-space data if weights are closer to 1. The reconstruction will recover data that have weights equal to or ~0 in the iterative reconstruction. This provides the benefit of a higher

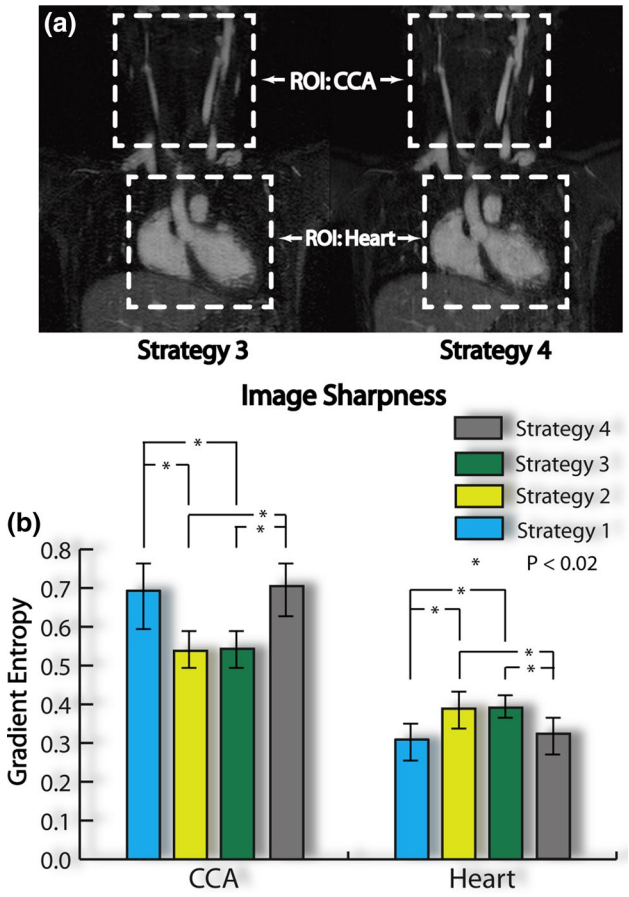

Fig. 4 **a** Reconstructed images for Strategies 3 and 4 demonstrate the two regions of interest (ROIs) where image sharpness was measured using gradient entropy. **b** Regional image sharpness of two ROIs [common carotid artery (CCA) and heart] using images reconstructed from four different strategies. In the static CCA, both Strategies 1 and 4 have significantly higher sharpness than Strategies 2 and 3 due to the lower undersampling factor. However, in the heart, where intracardiac structures are dynamic, Strategies 2 and 3 have significantly higher sharpness than Strategies 1 and 4 because of the higher effective temporal resolution and temporal footprint in the setting of complex cardiac motion

signal-to-noise (SNR) in the reconstruction due to the increased amount of data being incorporated. At the same time, this is not expected to affect image sharpness, since only data that have small weights will be recovered.

Since cardiac arrhythmia during image acquisition is not a common concern for pediatric CHD patients [32], the use of a symmetric flat-top, two-sided Gaussian kernel in the motion-weighted reconstruction is a practical choice for providing high-quality images to resolve cardiac motion, with greatly reduced computation requirements. In patients with irregular heartbeats, variations in cardiac cycles can lead to different motion range experienced by individual cardiac-phase segments in each heartbeat. If the shapes of the Gaussian kernels in motion-weighted reconstruction are simply scaled to meet the changes in cardiac cycle length, motion will still occur in reconstructed images when corresponding phase segments in each heartbeat are combined and used for reconstruction. This could potentially be addressed by changing the kernel shape for phase segments in irregular heartbeats so that data resides under the modified kernel will experience the motion to the same degree as those in regular heartbeats. This synchronization of motion range for different segments may reduce motion blurriness in the reconstructed image.

The remaining 2–3% error in LV functional measurement between high-temporal-resolution reconstructions and the 2D cine reference standard may be due to the different number of cardiac phases (18 phases for 4D ROCK-MUSIC and 25 for 2D cine) intrinsic for each technique. However, we have to also consider that 2D cine is acquired during (ventilator-controlled) breath-holding and 4D ROCK-MUSIC is acquired without breath-holding. It is possible that the remaining 2–3% error was due to the physiological effects of breath-holding.

In this work, we calculated global cardiac functional parameters (ESV, EDV, and EF) from the reformatted 2D slices even though 3D volumes are directly available from the ROCK-MUSIC data sets. This is mainly because the current reference ranges of these functional parameters were determined using 2D techniques. To accurately assess the performance of the different reconstruction strategies mentioned in this study and to obtain a fair comparison with the current gold standard 2D cine acquisition, we chose to obtain these functional parameters from reformatted 2D slices. However, we acknowledge that direct measurements from 3D volumes are possible, and the accuracy of such an approach is currently under investigation in our group.

Although the proposed motion-weighted reconstruction was demonstrated using ferumoxytol-enhanced MRA data sets, which usually have high SNR that allows highly accelerated techniques, the underlying methodology could also be applied to other cardiac-resolved data that have different SNR or contrast. Ferumoxytol is a US Food and Drug Administration (FDA)-approved intravenous iron supplement for iron-deficiency anemia and has been used off-label as an MRI contrast agent in both adults [33–36] and pediatric [7, 37–39] patients. In the pediatric congenital heart disease patient population, there is strong evidence that the use of ferumoxytol has highly favorable risk/benefit ratio, as demonstrated by Nguyen et al. [7]. At our center, the use of ferumoxytol has significantly changed the paradigm of cardiac MRI for pediatric congenital heart disease. Conventional cardiac MRI protocols for pediatric CHD include, among others, multiple 2D cardiac cine acquisitions, 3D first-pass contrast-enhanced MRA (CE-MRA), and phase-contrast flow imaging (PC-MRI). They are limited by the breath-holding period, the

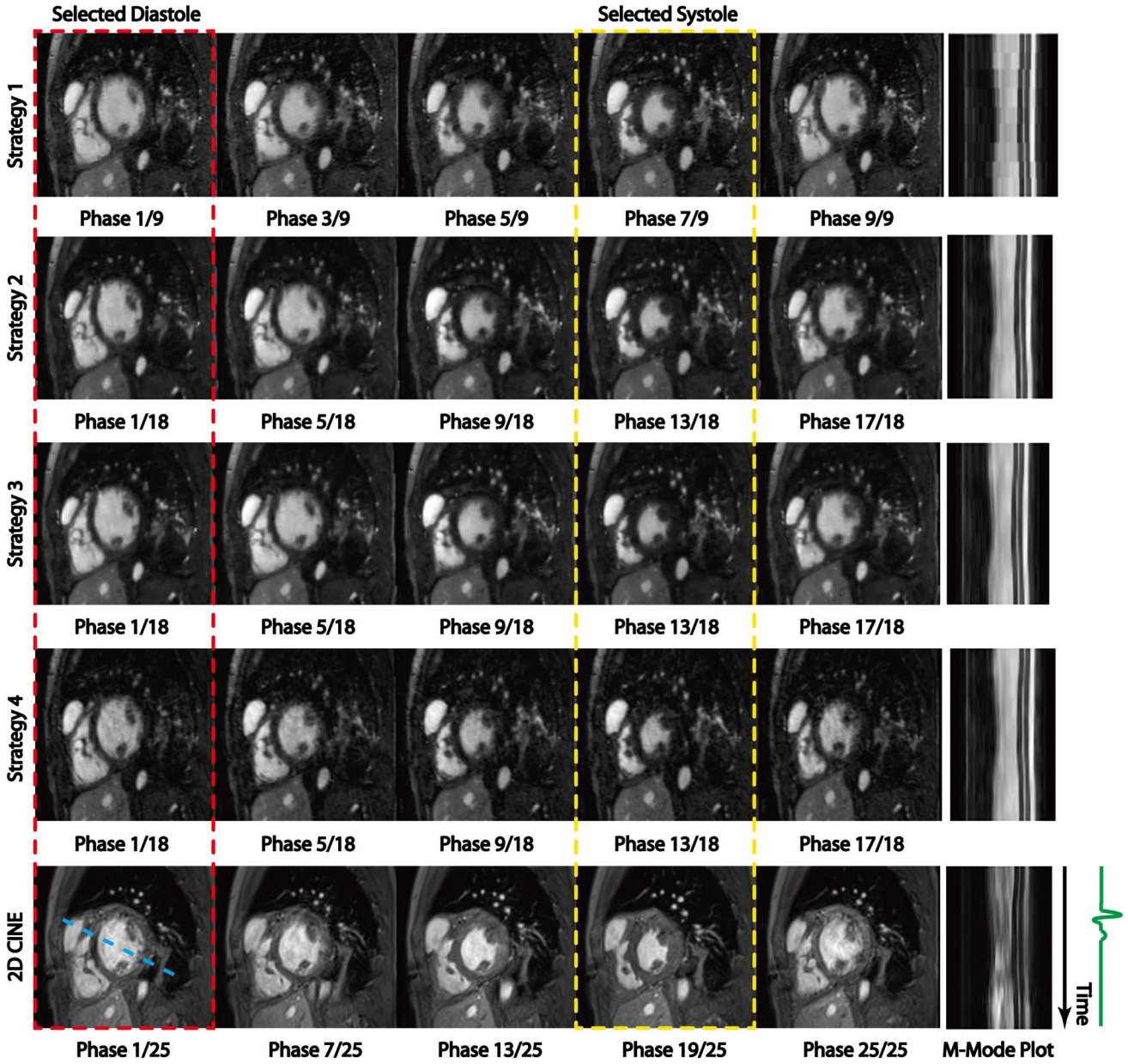

Fig. 5 Reformatted ventricular short-axis views of the heart from four reconstruction strategies and 2D cine. The M-mode plot to the right of the figure reflects the temporal resolution at the location of the dashed blue line for each of the different strategies. The temporal profile of Strategy 1 is coarse because of limited temporal resolution, whereas the temporal profiles of the other three strategies are smoother and similar to 2D cine. The selected end-diastole and end-systole phases for volumetric measurements are highlighted with red and yellow dashed boxes, respectively

need to capture the first pass of a contrast agent bolus, and relatively thick 2D slices in cardiac cine MRI. Moreover, the complex and highly variable anatomy seen in CHD patients often necessitates customized acquisition protocols directly supervised by a physician (cardiologist or radiologist) to specify geometrically appropriate imaging planes. The ferumoxytol MRI protocol used in this work essentially eliminated the aforementioned drawbacks of conventional cardiac MRI protocols.

Conclusion

We present a practical approach to doubling temporal resolution in 4D cardiac functional assessment in children based on a ROCK-MUSIC acquisition. Using

Table 2 Quantitative left-ventricular functional measurements

	ESV (ml)	EDV (ml)	EF (%)
Strategy 1	14.8 ± 5.0 (0.72)	34.3 ± 13.2 (0.83)	56.9 ± 8.2 (0.79)
Strategy 2	13.7 ± 4.2 (0.91)	34.5 ± 12.8 (0.96)	58.8 ± 9.4 (0.93)
Strategy 3	13.9 ± 5.3 (0.94)	34.8 ± 13.2 (0.98)	58.9 ± 9.0 (0.96)
Strategy 4	14.0 ± 5.1 (0.86)	34.4 ± 12.9 (0.92)	58.0 ± 8.6 (0.90)
2D cine	13.3 ± 4.8	35.1 ± 13.2	60.4 ± 9.0
Error: strategy 1 vs cine	8.4 ± 3.7%	− 1.9 ± 0.6%	− 6.8 ± 0.5%
Error: strategy 2 vs cine	3.3 ± 2.1%	− 0.9 ± 0.3%	− 2.6 ± 0.6%
Error: strategy 3 vs cine	3.5 ± 1.1%	− 0.8 ± 0.4%	− 2.7 ± 0.7%
Error: strategy 4 vs cine	4.1 ± 1.9%	− 1.2 ± 0.5%	− 3.5 ± 0.5%

Lin's correlation coefficients for measured volumes/ejection fraction between each strategy and the reference standard 2D cine images are in parentheses

ESV end-systolic volume, *EDV* end-diastolic volume, *EF* ejection fraction

motion-weighted reconstruction, LV quantitative measurements are significantly improved compared with the phase-by-phase reconstruction. At the same time, reconstruction time and computation memory requirements are modest compared with motion-regularized reconstructions.

Acknowledgements This work was supported by grant from the NIH R01HL127153.

Author contribution ZZ, FH, TY and PH conceived and designed the study, ZZ collected data; performed data analysis, interpretation; and drafted the manuscript. KLN, JPF, PH provided detailed review of the study design, results, and conclusions. All authors read, made critical revisions to, and approved the final manuscript.

Compliance with ethical standards

Conflict of interest All authors have no conflict of interest.

Ethical approval All procedures performed in studies involving human participants were in accordance with the ethical standards of the institutional and/or national research committee and with the 1964 Helsinki declaration and its later amendments or comparable ethical standards.

Informed consent Informed consent was obtained from all individual participants included in the study.

References

1. Ntsinjana HN, Hughes ML, Taylor AM (2011) The role of cardiovascular magnetic resonance in pediatric congenital heart disease. J Cardiovasc Magn Reson 13:51
2. Bailliard F, Hughes ML, Taylor AM (2008) Introduction to cardiac imaging in infants and children: techniques, potential, and role in the imaging work-up of various cardiac malformations and other pediatric heart conditions. Eur J Radiol 68:191–198
3. Fratz S, Chung T, Greil GF, Samyn MM, Taylor AM, Valsangiacomo Buechel ER, Yoo SJ, Powell AJ (2013) Guidelines and protocols for cardio-vascular magnetic resonance in children and adults with congenital heart disease: SCMR expert consensus group on congenital heart dis-ease. J Cardiovasc Magn Reson 15:51
4. Brown MD, Kallar SK (1985) Hypoxemia in children following general anesthesia in the ambulatory surgery center. Anesthesiology 63:A460
5. Han F, Rapacchi S, Khan S, Ayad I, Salusky I, Gabriel S, Plotnik A, Finn JP, Hu P (2015) Four-dimensional, multiphase, steady-state imaging with contrast enhancement (MUSIC) in the heart: a feasibility study in children. Magn Reson Med 74:1042–1049
6. Han F, Zhou Z, Han E, Gao Y, Nguyen KL, Finn JP, Hu P (2017) Self-gated 4D multiphase, steady-state imaging with contrast enhancement (MUSIC)using rotating cartesian K-space (ROCK): validation in children with congenital heart disease. Magn Reson Med 78:472–483
7. Nguyen KL, Han F, Zhou Z, Brunengraber DZ, Ayad I, Levi DS, Satou GM, Reemtsen BL, Hu P, Finn JP (2017) 4D MUSIC CMR: value-based imaging of neonates and infants with congenital heart disease. J Cardiovasc Magn Reson 19(1):40
8. Tsao J, Boesiger P, Pruessmann KP (2003) k-t BLAST and k-t SENSE: dynamic MRI with high frame rate exploiting spatiotemporal correlations. Magn Reson Med 50:1031–1042
9. Jung H, Sung K, Nayak KS, Kim EY, Ye JC (2009) k-t FOCUSS: a general compressed sensing framework for high resolution dynamic MRI. Magn Reson Med 61:103–116
10. Lustig M, Santos JM, Donoho DL, Pauly JM (2006) k-t SPARSE: high framerate dynamic MRI exploiting spatio-temporal sparsity. In: Proceedings of the 14th annual meeting of ISMRM, Seattle, Washington, USA, p 2420
11. Lingala SG, Hu Y, Dibella E, Jacob M (2011) Accelerated dynamic MRI exploiting sparsity and low-rank structure: k-t SLR. Trans Med Imaging 30:1042–1054
12. Otazo R, Candes E, Sodickson DK (2015) Low-rank plus sparse matrix decomposition for accelerated dynamic MRI with separation of background and dynamic components. Magn Reson Med 73:1125–1136
13. Feng L, Srichai MB, Lim RP, Harrison A, King W, Adluru G, Dibella EVR, Sodickson DK, Otazo R, Kim D (2013) Highly accelerated real-time cardiac cine MRI using k-t SPARSE-SENSE. Magn Reson Med 70:64–74

14. Kozerke S, Tsao J, Razavi R, Boesiger P (2004) Accelerating cardiac cine 3D imaging using k-t BLAST. Magn Reson Med 52:19–26
15. Adluru G, Awate SP, Tasdizen T, Whitaker RT, DiBella EVR (2007) Temporally constrained reconstruction of dynamic cardiac perfusion MRI. Magn Reson Med 57:1027–1036
16. Usman M, Atkinson D, Odille F, Kolbitsch C, Vaillant G, Schaeffter T, Batchelor PG, Prieto C (2013) Motion corrected compressed sensing for free-breathing dynamic cardiac MRI. Magn Reson Med 70:504–516
17. Feng L, Axel L, Chandarana H, Block KT, Sodickson DK (2016) Otazo R.XD-GRASP: golden-angle radial MRI with reconstruction of extra motion-state dimensions using compressed sensing. Magn Reson Med 75:775–788
18. Jiang W, Ong F, Johnson KM, Nagle SK, Hope TA, Lustig M, Larson PEZ (2017) Motion robust high resolution 3D free-breathing pulmonary MRI using dynamic 3D image self-navigator. Magn Reson Med 79:2954–2967
19. Cheng JY, Zhang T, Pauly JM, Vasanawala SS, Lustig M (2014) Free breathing dynamic contrast enhanced 3D MRI with resolved respiratory motion. In: Proceedings of the 22nd annual meeting of ISMRM, Milan, Italy, Abstract 330
20. Johnson KM, Block WF, Reeder SB, Samsonov A (2012) Improved least squares MR image reconstruction using estimates of K-space data consistency. Magn Reson Med 67:1600–1608
21. Forman C, Piccini D, Grimm R, Hutter J, Hornegger J, Zenge MO (2015) Reduction of respiratory motion artifacts for free-breathing whole-heart coronary MRA by weighted iterative reconstruction. Magn Reson Med 73:1885–1895
22. Cheng JY, Zhang T, Ruangwattanapaisarn N, Alley MT, Uecker M, Pauly JM, Lustig M, Vasanawala SS (2015) Free-breathing pediatric MRI with nonrigid motion correction and acceleration. J Magn Reson Imaging 42:407–420
23. Feng L, Huang C, Shanbhogue K, Sodickson DK, Chandarana H, Otazo R (2018) RACER-GRASP: respiratory-weighted, aortic contrast enhancement-guided and coil-unstreaking golden-angle radial sparse MRI. Magn Reson Med 80:77–89
24. Zhou Z, Han F, Rapacchi S, Nguyen KL, Brunengraber DZ, Kim GHJ, Finn JP, Hu P (2017) Accelerated ferumoxytol-enhanced 4D multiphase, steady-state imaging with contrast enhancement (MUSIC) cardiovascular MRI: validation in pediatric congenital heart disease. NMR Biomed. https://doi.org/10.1002/nbm.3663
25. Uecker M, Lai P, Murphy MJ, Virtue P, Elad M, Pauly JM, Vasanawala SS, Lustig M (2014) ESPIRiT-an eigenvalue approach to autocalibrating parallel MRI: where SENSE meets GRAPPA. Magn Reson Med 71:990–1001
26. Cheng JY, Hanneman K, Zhang T, Alley MT, Lai P, Tamir JI, Uecker M, Pauly JM, Lustig M, Vasanawala SS (2016) Comprehensive motion-compensated highly accelerated 4D flow MRI with ferumoxytol enhancement for pediatric congenital heart disease. J Magn Reson Imaging 43:1355–1368
27. Feng L, Coppo S, Piccini D, Yerly J, Lim RP, Masci PG, Stuber M, Sodickson DK, Otazo R (2018) 5D whole-heart sparse MRI. Magn Reson Med 79:826–838
28. Bernstein MA, King KF, Zhou XJ (2004) Handbook of MRI pulse sequences. Elsevier Academic Press, Amsterdam
29. Uecker M, Ong F, Tamir J, Bahri D, Virtue P, Cheng J, Zhang T, Lustig M (2015) Berkeley advanced reconstruction toolbox. In: Proceedings of the 23rd annual meeting of ISMRM, Toronto, Canada, vol 23, p. 2486
30. McGee KP, Manduca A, Felmlee JP, Riederer SJ, Ehman RL (2000) Image metric-based correction (autocorrection) of motion effects: analysis of image metrics. J Magn Reson Imaging 11:174–181
31. Li Lin (1989) A concordance correlation coefficient to evaluate reproducibility. Biometrics 45:255–268
32. Turner CJ, Wren C (2013) The epidemiology of arrhythmia in infants: a population-based study. J Paediatr Child Health 49:278–281
33. Li W, Tutton S, Vu AT et al (2005) First-pass contrast-enhanced magnetic resonance angiography in humans using ferumoxytol, a novel ultrasmall superparamagnetic iron oxide (USPIO)-based blood pool agent. J Magn Reson Imaging 21:46–52
34. Bashir MR, Mody R, Neville A et al (2014) Retrospective assessment of the utility of an iron-based agent for contrast-enhanced magnetic resonance venography in patients with end stage renal diseases. J Magn Reson Imaging 40:113–118
35. Prince MR, Zhang HL, Chabra SG, Jacobs P, Wang Y (2003) A pilot investigation of new superparamagnetic iron oxide (ferumoxytol) as a contrast agent for cardiovascular MRI. J Xray Sci Technol 11:231–240
36. Sigovan M, Gasper W, Alley HF, Owens CD, Saloner D (2012) USPIO-enhanced MR angiography of arteriovenous fistulas in patients with renal failure. Radiology 265:584–590
37. Nayak AB, Luhar A, Hanudel M et al (2015) High-resolution, whole-body vascular imaging with ferumoxytol as an alternative to gadolinium agents in a pediatric chronic kidney disease cohort. Pediatr Nephrol 30:515–521
38. Ruangwattanapaisarn N, Hsiao A, Vasanawala SS (2015) Ferumoxytol as an off-label contrast agent in body 3 T MR angiography: a pilot study in children. Pediatr Radiol 45:831–839
39. Thompson EM, Guillaume DJ, Dosa E et al (2012) Dual contrast perfusion MRI in a single imaging session for assessment of pediatric brain tumors. J Neurooncol 109:105–114